



UNIVERSITY OF LEEDS

MSC INDIVIDUAL REPORT

Experimental and Numerical Modelling of Coastal Processes

Author:

Thomas GOODFELLOW

Supervisors:

Prof. Onno BOKHOVE

Dr. Duncan BORMAN

ABSTRACT:

Coastal risk management consultants JBA Group required a wave tank capable of illustrating certain coastal processes. The tank was designed to demonstrate overtopping on different coastal defence structures. Simulations were made of the Navier-Stokes equations using Smoothed Particle Hydrodynamics (SPH) and Finite Element Methods (FEM). Exact linear solutions for these models were used to verify these two codes. Simulations of these models were compared with experimental measurements of the physical model wave tank.

MECH5870M Team Project:
Wave Tank Building for Coastal Processes

Student: Thomas Goodfellow

Supervisors: Prof. Onno Bokhove

Dr. Duncan Borman

20/04/2015

Contents

1	Introduction	1
1.1	Aims and Objectives	1
1.2	Waves and Wave Generation	2
1.3	Coastal Processes	4
1.4	Coastal Defences	5
1.5	Scaling	6
2	Theory	7
2.1	Analytic Solutions	7
2.1.1	Natural Frequencies and Dispersion Relation	9
2.1.2	Exact Solution	10
2.1.3	Forced Standing Wave	11
2.2	EurOtop	12
2.3	Smoothed Particle Hydrodynamics	14
3	SPH Validation	15
3.1	Numerical Damping	15
3.1.1	Energy	16
4	Experimental Design	18
4.1	Tank and Defences	18
4.2	Wave Maker	20
4.2.1	Mechanical Design	20
4.2.2	Control System	22
4.3	Image processing	25
4.4	Experimental Design	25

5 Results and Discussion	26
5.1 Conclusions	30
A Coastal Defences	34
B Wood Paddle	35
C Paddle Hinged at Bottom	36
D Improved Wave Maker	37
E Simple Arduino Program	38
F Encoder Code	40
G Final Design and Extra Defences	41

Chapter 1

Introduction

JBA group is an environmental, engineering and risk group who works actively in the area of coastal risk management. JBA Trust, a not-for-profit subsidiary of JBA group, work to support and promote scientific research, education and training in the areas of environmental risk and resourcing (JBA, 2015). JBA Trust proposed a project to design and build a wave tank which could be used to demonstrate key coastal processes such as overtopping. The wave tank was to be supported by theoretical and numerical models. Smoothed Particle Hydrodynamics (SPH) and Finite Element (FE) Methods were used to model the water waves and a comparison was made to results obtained from experiments.

1.1 Aims and Objectives

The author's aim in the project was to develop a method of generating waves in the tank, involving the detailed design and manufacture of wave makers, control systems and drive mechanisms. Time was also spent deriving analytic solutions, investigating numeric results and obtaining experimental data. Objectives included setting up an experimental tank, designing coastal defences and testing wave makers with these defences. Wave conditions able to produce required overtopping and the methods of producing these were investigated. Analytic solutions were used to verify the numerical models and to compare against experiments performed using the tank. The main project deliverable was a wave tank design to be manufactured by HydroTec – a local modelling consultancy – and would be a culmination of strengths and limitations revealed through extensive testing of the experimental tank and wave maker, especially when overtopping occurs.

1.2 Waves and Wave Generation

Surface waves seen in the Ocean may be classified in terms of a wave period as suggested by Munk (1950). Wind generated waves in particular may be divided as:

Classification	Period
Capillary waves	less than 0.1 sec.
Ultra-gravity waves	from 0.1 sec. to 1 sec.
Ordinary gravity waves	from 1 sec. to 30 sec.

Capillary waves are influenced by surface tension more than by gravity and regularly manifest themselves in small ponds, for instance. When the water is particularly shallow, such as in a scaled model, surface tension forces may become significant and produce unwanted capillary waves. Therefore a distorted model is often used in wave tank design, as discussed in Section 1.5. Ultra-gravity and ordinary gravity waves are of interest in coastal modelling, in which gravity rather than surface tension is the predominant restoring force.

A wave can be described in terms of a wavelength λ , period T , frequency ω , amplitude h and still-water depth H . Waves can also be classified in terms of the ratio of wavelength to water depth, λ/H . As these values change, so does the motion of water particles in the fluid. For instance, at small λ/H , i.e. in deep water, the motion of particles is circular in nature. As this ratio is reduced (shallow water) the particle motion becomes more elongated due to the effects of the bottom surface Hofmann (2008). This is shown in Figure 1.1 from Hofmann (2008), adapted from Ippen and Eagleson (1966). Note that the image used different notation to that adopted in this report.

An articulating flap is often used to generate waves in model tanks. These come in many different forms according to the types of waves desired. For instance deep water waves may be produced using a paddle hinged at the bottom of the tank to approximate the particle motion. Similarly a piston paddle would best approximate the particle motion in shallow water waves, as shown in Figure 1.2 (Edinburgh Designs, 2015). More complex forms of wave generator may be designed such as flexible flap, multi-flap, suspended paddles and plungers; many such examples were provided by Chappell (1953).

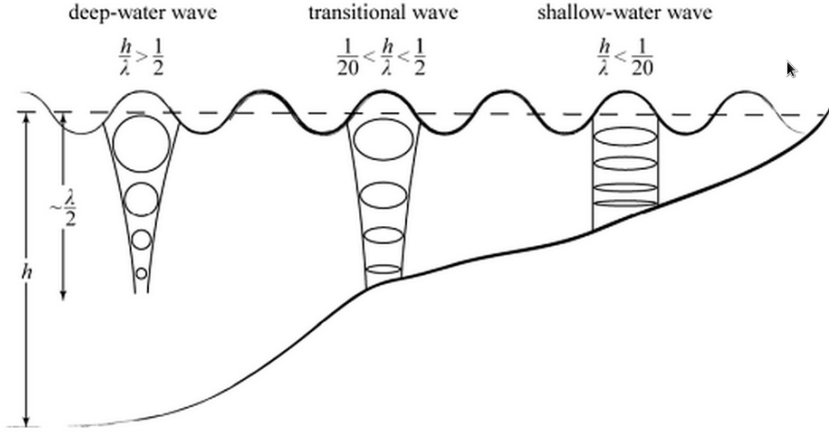


Figure 1.1: Particle motion in waves with different water height to wavelength ratio.

A design of particular interest is the single pivoting paddle due to its relative mechanical simplicity providing a constant period wave. This paddle may be hinged at the bottom of the tank, or above the free surface. As noted previously, paddles hinged at the bottom of the tank are well-suited to producing deep water waves. A paddle above the free surface would be more akin to a piston wave-maker, therefore more appropriate to shallow water waves. However the latter design is less satisfactory from the viewpoint of simulating particle motion as it attempts to increase orbits with depth (Straub and Pilch, 1953). Furthermore leakage around the bottom of the paddle may result in smaller amplitudes compared to a piston wavemaker. Regardless, design limitations such as space, available materials or a moving bed may require the rigid flap to be fixed above the free surface.

A final consideration is reflected waves. Naturally, waves reflected off structures would be dissipated out into the ocean. However in a model tank waves are reflected back towards the wave generator which itself is highly reflective. Methods of attenuating this include a filter in front of the wave generator (Biesel, 1948), pneumatic wave generators (Keulegan, 1966) and blowing a high energy air stream in the direction of waves as used in Delft Hydraulic Laboratory in the Netherlands. Pneumatic wave generators aspirate water into a chamber and let it fall freely downwards. This means no articulating flaps are used and so a slope may be implemented above and around the chamber, absorbing any reflected waves. A high energy air stream above the surface would act to aid outgoing waves and damp incoming waves, reducing reflection. More advanced methods include positive feedback loops which adjust the control to absorb waves as they return.

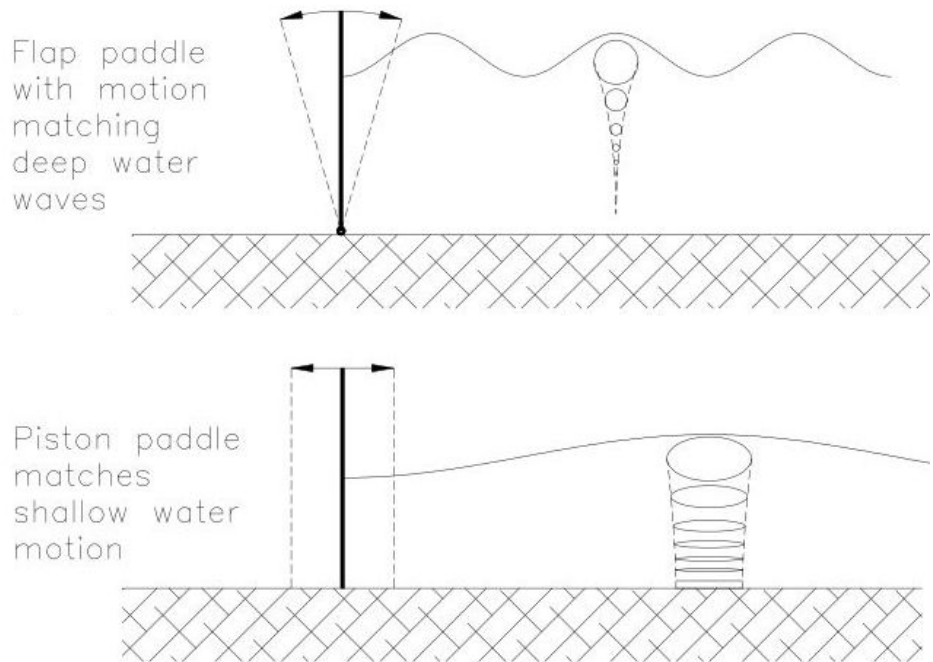


Figure 1.2: Waveforms obtained using hinged and piston wave generators.

1.3 Coastal Processes

As sea waves attack coastal defences such as dykes and seawalls, excess water may splash up and over the defence, particularly during storms. This is known as overtopping and can pose a flood risk to nearby areas when the rate of discharge is high. ‘Green water’ overtopping occurs when the run-up level of a wave on a seawall is high, and a continuous sheet of water passes over the crest of the structure (HR Wallingford, 2007). A second form of overtopping occurs when waves are impulsive, i.e. when waves break on the face of the seawall and produce significant volumes of splash.

When designing sea defences it is important to be able to predict the amount of overtopping around a structure. Indeed this has garnered substantial interest in the past from researchers worldwide. Tsuruta and Goda (1968) published a paper in Japan introducing a concept of expected wave overtopping rate by averaging experimental overtopping with expected discharge based on a wave height histogram. Separately in the UK the first predictions of overtopping were presented by Owen (1980) based on wave tests. These studies formed the basis of further tests world wide, leading to a variety of prediction tools based on empirical data Goda (2010).

Modern industrial standard tools used to calculate overtopping include EurOtop (HR Wallingford, 2007), which is a semi-analytic method using equations derived empirically from research studies around Europe and further overseas. The overtopping neural network developed by Deltares (2015) is a second prediction tool which differs from EurOtop in that it works by interpolating between many experimental results obtained for similar structures to that defined. Both tools are used by JBA to evaluate the risk of overtopping for different structures and conditions around the UK and overseas.

1.4 Coastal Defences

Defences range from simple vertical seawalls to complex composite structures and off-shore breakwaters. Some common coastal defences include: vertical walls, slopes, re-curves, rock defences and composite structures. Vertical walls have a small footprint compared to most other defences, however they are very reflective. This can result in increased beach scour and erosion next to the defence, causing potential structural failure while also leading a deterioration in boating or swimming conditions seaward of the wall (Thomas and Hall, 1992). Furthermore when impacted by severe waves, the volume of water splash can be very large, even carrying sand and other materials with it. Sloped seawalls can act to dissipate some of the wave energy leading up to the crest of the structure, however they can sometimes result in more overtopping as revealed in section 2.2 of this report. In addition to smooth sloped structures, personal discussions with Daniel Rodger and Emma Rendle at JBA consulting revealed that stepped slopes are often used as coastal defences. These structures dissipate energy over each step and so drastically reduce the energy in the wave by the time it reaches the crest. They are also no as unsightly and may be used as seating by the public in low-tide.

Rock defences utilise large boulders to dissipate energy, much like a stepped structure. A re-curve, or wave return wall, are structures at the crest of a sea defence which curve and deflect up-rushing water seawards, reducing overtopping. They are most effective at the end of a smooth slope such that water flows smoothly up and around the structure (Thomas and Hall, 1992). This may not work with rock defences or steps may due

to a more turbulent run-up of water, however it must be remembered that these structures produce less run-up in the first place. Composite structures are a combination of a number of defenses, for instance a rocky slope leading up to a flat berm, into a second, smooth slope with a re-curve at the top. These may be tailored to a particular location and conditions to optimally reduce the amount of overtopping.

1.5 Scaling

Before designing the tank, consideration was given to the effect of scale on the wave conditions. It was important to model ocean waves as accurately as possible, however the constraints of the tank meant that a geometrically distorted model was required. This is because horizontal length scales tend to be much larger than vertical length scales in coastal engineering problems. If the model was scaled directly the water could be extremely shallow such that surface tension forces dominated and capillary waves were produced (Lighthill, 1978). Data obtained in experiments would not be compared to data obtained from monitor buoys in the ocean. Therefore it was not of paramount importance that waves in the tank matched those in real conditions; rather that it was visually representative of overtopping. Therefore a geometrically distorted model could be used with confidence, providing overtopping was realistic.

A study was performed by Van Alwon (2015) to compare similarity between model and real life conditions. It was determined that a water height of 70 mm was sufficient to avoid capillary waves while preventing water from splashing out of the tank. Equations were then derived by Van Alwon (2015) and used to determine typical real life conditions represented by those in the tank. Froude and Reynolds criteria were also used to assess similarity between prototype and model, with good agreements found.

Chapter 2

Theory

Initial insight into the problem was revealed through linear wave theory – a well established theory governing surface gravity waves. The result was a set of analytical equations describing the evolution of waves in an enclosed tank. Linear results for basic conditions could then be used to verify the numerical models.

2.1 Analytic Solutions

The Navier-Stokes equations are known to describe the motion of viscous fluids. This includes the continuity equation, derived by considering the conservation of mass in a system; the net mass of fluid entering or leaving an arbitrary region over time is equal to the rate of change of mass inside the volume:

$$\frac{\partial}{\partial t} \int_V \rho dV + \int_S \rho \mathbf{u} \cdot d\mathbf{S} = 0. \quad (2.1)$$

This can be expressed in differential form as

$$\frac{\partial \rho}{\partial t} + \nabla \cdot (\rho \mathbf{u}) = 0, \quad (2.2)$$

where ρ is fluid density and \mathbf{u} is velocity. Note that if the fluid is incompressible, i.e. density ρ is constant then (2.2) may be written as

$$\nabla \cdot \mathbf{u} = 0. \quad (2.3)$$

Furthermore if there is no vorticity generation, i.e. \mathbf{u} is irrotational then the velocity can be written as the gradient of a scalar field:

$$\mathbf{u} = \nabla \phi, \quad (2.4)$$

where ϕ is the velocity potential. Then using (2.3) the incompressible, irrotational flow of fluid in a closed tank is governed by the Laplace equation:

$$\nabla^2 \phi = 0 \quad \text{in } X \in [0, L] \cup [0, -H_0] \quad (2.5)$$

with the boundaries,

$$\partial_t \eta = \partial_z \phi \quad \text{at } z = 0 \quad (2.6)$$

$$\partial_t \phi = -g\eta \quad \text{at } z = 0 \quad (2.7)$$

$$\partial_z \phi = 0 \quad \text{at } z = -H_0 \quad (2.8)$$

Where η is the position of the free surface. Solutions are assumed to be harmonic so

$$\eta \propto e^{-i\omega t} \text{ and } \phi \propto e^{-i\omega t}.$$

Analysis was restricted to the 2D vertical plane as there was assumed to be no flow in the y-direction. The velocity potential was then given by functions of x and z only, so we seek separable solutions of form

$$\phi = F(x)G(z)e^{-i\omega t},$$

$$\nabla^2 \phi = \partial_{xx} \phi + \partial_{zz} \phi = 0.$$

Therefore

$$GF'' + FG'' = 0 \text{ and } \frac{F''}{F} = -\frac{G''}{G} = \kappa^2,$$

where κ^2 is a constant chosen to represent trigonometric solutions in x and exponential solutions in z , i.e. motion is repeating sinusoidal along the tank but varies exponentially with height. Then:

$$G'' - \kappa^2 G = 0 \text{ and } F'' + \kappa^2 F = 0. \quad (2.9)$$

So if $G \propto e^{\lambda z}$, then $\lambda^2 = \kappa^2$ and $\lambda = \pm\kappa$.

$$\Rightarrow G = Ae^{\kappa z} + Be^{-\kappa z}. \quad (2.10)$$

This equation is bounded as $\partial_z \phi = G' = 0$ on $z = -H_0$, so

$$\kappa A e^{-\kappa H_0} - B^{\kappa H_0} = 0 \implies B = A e^{-2\kappa H_0}$$

and

$$G = A(e^{\kappa z} + e^{-\kappa z - 2\kappa H_0}) = \tilde{A}(e^{\kappa(z+H_0)} + e^{-\kappa(z+H_0)}) = \tilde{A} \cosh \kappa(z + H_0).$$

Dropping the tilde,

$$G = A \cosh \kappa(z + H_0). \quad (2.11)$$

Similarly, $F = e^{\gamma x}$, so $\gamma^2 + \kappa^2 = 0$ and $\gamma = \pm i\kappa$. So,

$$F = \tilde{A}e^{i\kappa x} + \tilde{B}e^{-i\kappa x} = A \cos \kappa x + B \sin \kappa x. \quad (2.12)$$

This equation is bounded on the side walls, $F' = u = \partial_x \phi = 0$ at $x = 0, x = L$ meaning

$$F' = -A\kappa \sin \kappa x + B\kappa \cos \kappa x = 0 \text{ at } x = 0. \quad (2.13)$$

So $B = 0$ and the equation for the velocity potential becomes

$$\phi = A \cos \kappa x \cosh \kappa(z + H_0)e^{-i\omega t}, \quad (2.14)$$

where A is some complex function.

2.1.1 Natural Frequencies and Dispersion Relation

It is known that $F' = 0$ at $x = L$ so

$$-A\kappa \sin \kappa L = 0 \implies \kappa = \frac{m\pi}{L} \quad (2.15)$$

for integer m . These are the natural frequencies of standing waves in the tank. Furthermore, differentiating the dynamic boundary condition (2.7) with time and combining with the kinematic condition (2.8) gives

$$\begin{aligned} \partial_{tt}\phi &= -g\partial_t\eta = -g\partial_z\phi \\ \partial_z\phi &= A\kappa \cos \kappa x \sinh \kappa(z + H_0)e^{-i\omega t}. \end{aligned}$$

So

$$\partial_z\phi|_{z=0} = A\kappa \cos \kappa x \sinh \kappa H_0 e^{-i\omega t}.$$

Combining with $\partial_{tt}\phi$,

$$\begin{aligned} -\omega^2 A \cos \kappa x \cosh \kappa H_0 e^{-i\omega t} &= -g A \kappa \cos \kappa x \sinh \kappa H_0 e^{-i\omega t} \\ \Rightarrow \omega^2 &= g \kappa \frac{\sinh \kappa H_0}{\cosh \kappa H_0} = g \kappa \tanh(\kappa H_0), \end{aligned} \quad (2.16)$$

which is the dispersion relation for a finite depth fluid. Figure 2.1 shows the dispersion relation plotted as frequency against wavenumber where the points indicate wavenumbers with integer n , corresponding to standing wave frequencies.

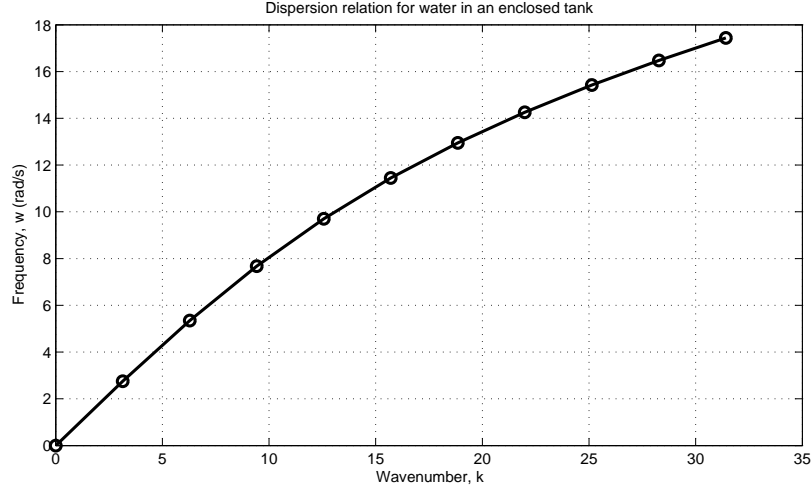


Figure 2.1: Dispersion relation with points indicating natural frequencies

2.1.2 Exact Solution

An exact solution for water surface η is obtained by taking the time derivative of the velocity potential (2.14):

$$\phi = A \cos \kappa x \cosh \kappa H_0 (\cos \omega t - i \sin \omega t)$$

$$\eta = -\partial_t \phi|_{z=0} = \frac{\omega}{g} A_R \cos \kappa x \cosh \kappa H_0 \sin \omega t - \frac{i\omega}{g} A_I \cos \kappa x \cosh \kappa H_0 \cos \omega t, \quad (2.17)$$

where A_R and A_I are the real and imaginary parts of A respectively. Taking the real part of the solution only,

$$\eta = B \cos \kappa x \cosh \kappa H_0 \sin \omega t, \quad (2.18)$$

where $B = \omega A_R / g$ is the amplitude of the wave. Taking a value of $H_0 = 0.07m$ as in the wave tank, $L = 1.5m$ and $B = 1/100H_0 = 0.7 \times 10^{-3}m$ then κ is chosen to produce a standing wave (2.15):

$$\kappa = \frac{m\pi}{L} = \frac{\pi}{1.5}$$

for the lowest frequency mode with $m = 1$. Then from the dispersion relation (2.16),

$$\omega = \sqrt{g\kappa \tanh \kappa H_0} = 6.58 \text{ rad/s} \quad (2.19)$$

The value of η was added onto the rest height of the fluid and plotted through time. A snapshot is shown in Figure 2.2 with an amplitude of 0.05 m and wavenumber $k = \pi/L$.

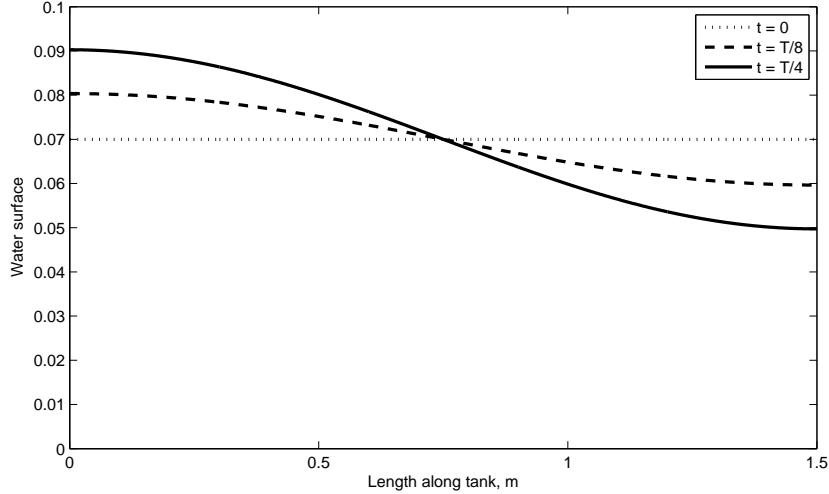


Figure 2.2: Standing wave solution in the tank at different time periods

2.1.3 Forced Standing Wave

We can now modify one of the boundary conditions such that the position of a piston wavemaker, \mathbf{x} is given by $\mathbf{x} = \alpha \sin \sigma t$ where α and σ are the wavemaker's amplitude and frequency respectively. The velocity of the wavemaker is then given by $\partial_x \phi = \alpha \sigma \cos \sigma t$.

We now assume that the solutions oscillate in phase with the wavemaker so that we now have

$$\eta \propto e^{-i\sigma t} \text{ and } \phi \propto e^{-i\sigma t}.$$

Using separation of variables it is observed that the solution form for the function $G(z)$ is precisely the same as the stationary standing wave case. We now reconsider the case for the function $F(x)$

$$F = \tilde{A}e^{i\kappa x} + \tilde{B}e^{-i\kappa x} = A \cos \kappa x + B \sin \kappa x. \quad (2.20)$$

The boundary conditions on x are now $\partial_x \phi = \alpha \sigma$ at $x = 0$ and $\partial_x \phi = 0$ at $x = L$ and we see that the derivative is still

$$F' = -A\kappa \sin \kappa x + B\kappa \cos \kappa x. \quad (2.21)$$

We must then solve the following linear system

$$\begin{bmatrix} 0 & \kappa \\ -\kappa \sin \kappa L & \kappa \cos \kappa L \end{bmatrix} \begin{bmatrix} A \\ B \end{bmatrix} = \begin{bmatrix} \alpha \sigma \\ 0 \end{bmatrix}.$$

This yields the two constants $B = \alpha \sigma / \kappa$ and $A = \alpha \sigma / (\kappa \tan \kappa L)$. The equation for velocity potential is now

$$\phi = \frac{\alpha \sigma}{\kappa} \left(\frac{\cos \kappa x}{\tan \kappa L} + \sin \kappa x \right) \cosh \kappa(z + H_0) e^{-i\sigma t}, \quad (2.22)$$

with a free surface, around $z = 0$, described by

$$\eta = -\frac{1}{g} \partial_t \phi \Big|_{z=0} = \frac{\alpha \sigma^2}{\kappa} \left(\frac{\cos \kappa x}{\tan \kappa L} + \sin \kappa x \right) \cosh \kappa H \sin \sigma t. \quad (2.23)$$

Where the gravity term is included in the amplitude α . Recalling that wavenumber is given by $k = n\pi/L$ then the $1/\tan \kappa L$ term in (2.23) provides an infinite solution for integer n . Physically, when the wavemaker is forced at the natural frequency the system is in resonance and unstable standing waves are produced.

Figure 2.3 shows a plot of free surface height against integer n from the wavenumber equation at a distance of $x = 0.5L$ along the tank. It can indeed be seen that the solution approaches infinity when forced at the natural frequency, $n = 2$. Note however that at $n = 1$ and 3 the solution is zero, this is because the mid point of the tank becomes an anti-node at odd integers as expected.

2.2 EurOtop

EurOtop is an industry standard tool used to approximate the overtopping on coastal defences using empirically derived equations. It was known that the largest deviations using EurOtop would be found for small overtopping discharges, therefore it would not be appropriate to calculate discharge in the prototype tank (HR Wallingford, 2007). However insight could be found on the variation in expected overtopping with different structures. Van der Meer et al. (2013) provided an empirical trend for the non-dimensional overtopping of water on a structure with different slopes. This trend was known to approximate discharge to a reasonable accuracy and was given by.

$$\frac{q}{\sqrt{gH_{m0}^3}} = a \exp \left(-\left(b \frac{R_c}{H_{m0}^3} \right)^c \right), \quad (2.24)$$

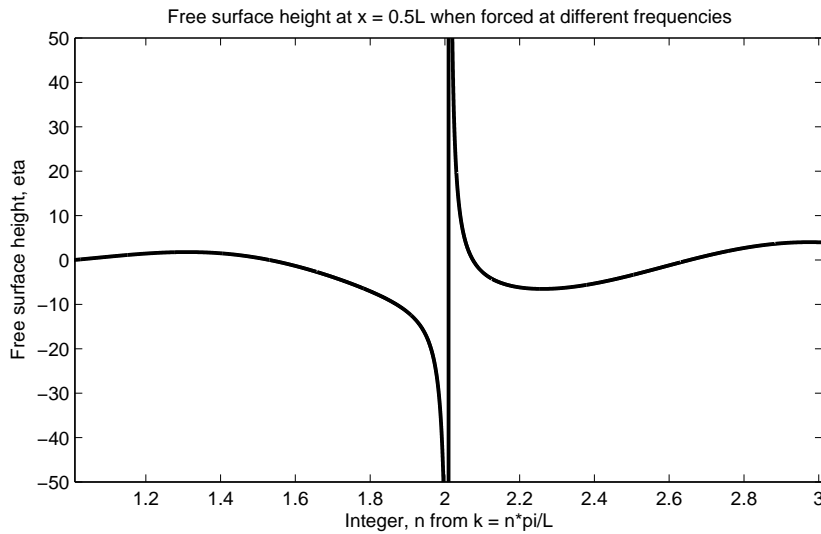


Figure 2.3: Free surface height at the tank mid-point for different wavenumbers

where q is discharge in m^3s^{-1} , the term on the left is dimensionless discharge, $c = 1.3$ was a constant taken to fit the trend, and a and b were constants given by:

$$a = 0.09 - 0.01(2 - \cot \alpha)^{2.1} \quad \text{where } a = 0.09 \text{ if } \cot \alpha > 2,$$

$$b = 1.5 + 0.42(2 - \cot \alpha)^{1.5} \quad \text{where } b_{max} = 2.35 \text{ and } b = 1.5 \text{ if } \cot \alpha > 2.$$

Figure 2.4 a.) shows a plot of constants a and b as a function of $\cot \alpha$. The constants were used to calculate overtopping with (2.24) and plotted against slope angle, α as shown in Figure 2.4 b.)

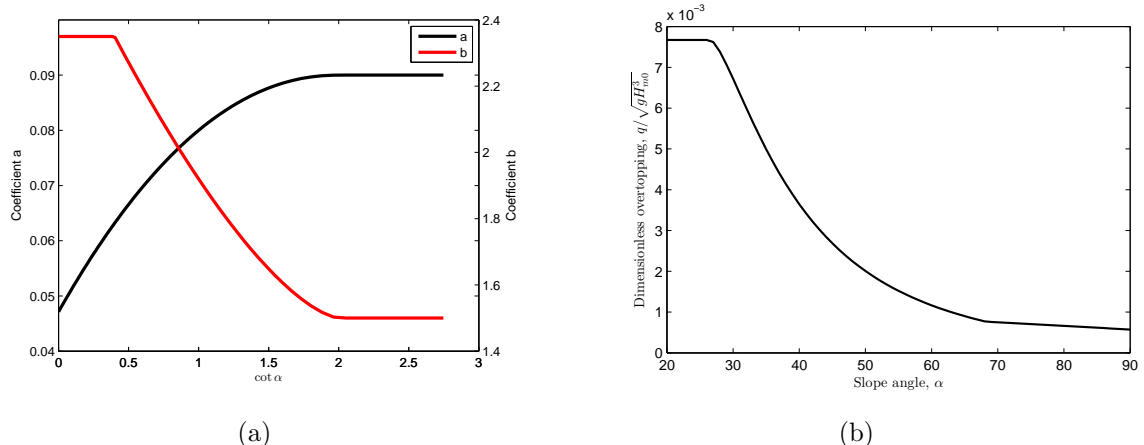


Figure 2.4: a.) Constants a and b with $\cot \alpha$. b.) Dimensionless overtopping with slope angle, α .

It could be seen that as the slope angle was increased from 20° up to 90° (vertical), less overtopping was predicted. This indicated that adding a sloping defense to a vertical structure increases the amount of overtopping observed.

2.3 Smoothed Particle Hydrodynamics

The wave tank was numerically modelled using the open source Smoothed Particle Hydrodynamics (SPH) software DualSPHysics. SPH is a meshless, Lagrangian, fluid particle modelling method particularly well suited to free surface problems (Gomez-Gesteira et al., 2010). The properties are approximated by an integral involving a weighting function, or kernel. This kernel defines a smoothing length for each particle, so the solution is calculated proportionally according to properties of nearby particles – a Lagrangian formulation. A full description of the equations and references are collected by Gomez-Gesteira et al. (2012).

Simulation times are typically longer than for mesh based methods, however it does have the benefit that calculations are not performed in empty areas, only areas where particles are. This has the potential to save on computational cost depending on the number of particles and formulations used.

Chapter 3

SPH Validation

The SPH code was validated for different problems, and was shown to perform well when modelling wave breaking (Dalrymple and Rogers, 2006), dam-break behaviour (Crespo et al., 2008) and in particular, wave-structure interaction (Gomez-Gesteira and Dalrymple, 2004). However numerical damping in the system was known to affect wave propagation. Therefore test cases based on analytic solutions were used to validate the SPH model, and investigate the level of damping present. Adjustments were then made to the model in an attempt to reduce the amount of damping and also reach particle independence. Details of which are found in the report by Van Alwon (2015).

3.1 Numerical Damping

Simulations were performed to compare SPH solutions with the linear unforced standing wave solution derived in Section 2.1.2 at low amplitude. This allowed the scale of the damping to be evaluated and determine whether it was within an acceptable range. To achieve this it was necessary to specify the starting position of particles in DualSPHysics such that the initial velocity was zero at time, $t=0$. It was known that potential energy would be a maximum, with zero kinetic energy and thus zero velocity, at $t = T/4$ where T is the period, i.e. when fluid is at maximum displacement. This was shown in Figure 2.2 in Section 2.1.2. The position of the free surface at $t = T/4$ was thus calculated using the exact solution and the fluid profile was reproduced in a 3D CAD package to create a .stl file. This file was then imported into DualSPHysics and scaled to fit the domain as shown in Figure 3.1, producing the required standing wave.

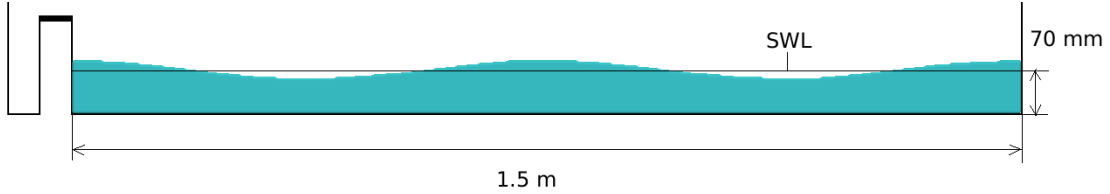


Figure 3.1: Initial conditions in DualSPHysics for an unforced solution.

3.1.1 Energy

The damping was analysed using the free surface heights extracted from the simulation. It was known that the total energy in the system was composed of kinetic and potential energy, and at maximum displacement the velocity was zero, thus no kinetic energy. Therefore the potential energy was calculated at maximum displacement every half-period for the exact solution and for three different particle distances to investigate the level of damping. In reality the energy would fluctuate between zero and the maximum value through time, however it would be impractical to investigate this trend and so only the energy at maximum displacement was evaluated. The potential energy was found using

$$PE = \frac{1}{2} \left(\int_0^L \eta^2 \right), \quad (3.1)$$

where η is fluid displacement from rest. This was evaluated numerically using the trapezium rule. Figure 3.2 shows the energy in the fluid at different time periods. The energy followed the same pattern regardless of particle distance, and for each case it levelled out at around 5 periods. As expected, the linear solution experienced no loss in energy. The solutions also began to diverge after levelling out, except for that with 2 mm particle distance. This was because simulations with 2 mm particle distance had been calibrated to remain in hydrostatic balance, whereas the other two had not. This was shown in the report by Van Alwon (2015). Furthermore the larger particle distance resulted in a higher fluid height at the beginning, thus increasing the energy. This was likely due to a larger kernel smoothing length resulting in a higher mass recorded above the free surface profiles.

The peaks observed in the data were due to the fact that solutions were obtained from SPH at 0.1 s increments, whereas the period was roughly 0.95 s. So at certain times the free surface would have been measured just before or after the peak height. This effect could be reduced by monitoring the solution at a smaller time increment, though doing

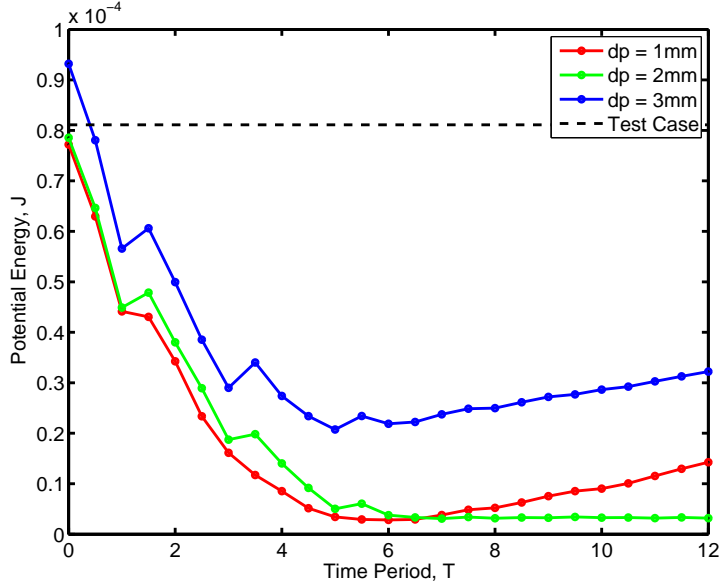


Figure 3.2: Potential energy in the fluid for different particle distances compared to analytic solution.

so would increase the size of the output files produced and was considered unnecessary. Of more interest was determining whether the rate of damping was the same regardless of particle distance. This was investigated using the L₂-norm, given by:

$$L^2 = \left(\int_0^{T_f} (e - F)^2 dt \right)^{\frac{1}{2}} \quad (3.2)$$

Where e is value of the exact solution at time t, and F is the value of the computed solution at period T. Table 3.1 shows the value of the L₂-norm for each particle distance. The values did not converge, indicating that changing the particle spacing also required a

Table 3.1: L^2 -norm for different particle distances

Particle Distance:	1 mm	2 mm	5mm
L ₂ -norm ($\times 10^{-4}$):	2.929	2.957	2.208

calibration to ensure hydrostatic balance. However in each case the rate of damping was similar indicating that another source of numerical damping was responsible as opposed to particle spacing. The fact that the energy in the system had damped by half over 2 time periods suggested that the simulations may not accurately represent conditions in the tank.

Chapter 4

Experimental Design

An experimental wave tank was used to test different wave maker designs and coastal defences with the aim of producing a design for a tank to be manufactured professionally by a local company, Hydrotec Consultants Ltd. The features of the tank were determined through scaling considerations, research into coastal defence design and wave maker technology. In particular three wave makers were manufactured and tested before deciding on a good design for the tank and its intended use.

The experimental tank, once designed, was used to obtain data on overtopping around different structures for comparison with numerical results. Overtopping was measured by collecting water over time behind the coastal defence, while image processing was used to capture the free surface position.

4.1 Tank and Defences

The deliverable wave tank was required to fit inside a particular vehicle for transportation which was measured prior to producing any concepts. The tank was limited to a length of 1.5 m, therefore the open-ended experimental tank was blocked off at 1.5 m using modelling foam. This material was chosen as it was easy to manipulate into different shapes, and so would be useful for manufacturing coastal defences. A single block was produced which was slightly larger than the width of the tank and wedged in at 1.5 m to aid with sealing. The seal was then made watertight using clear, weatherproof tape. The dimensions of the tank were X mm x Y mm x 1.5 mm (W x D x L).

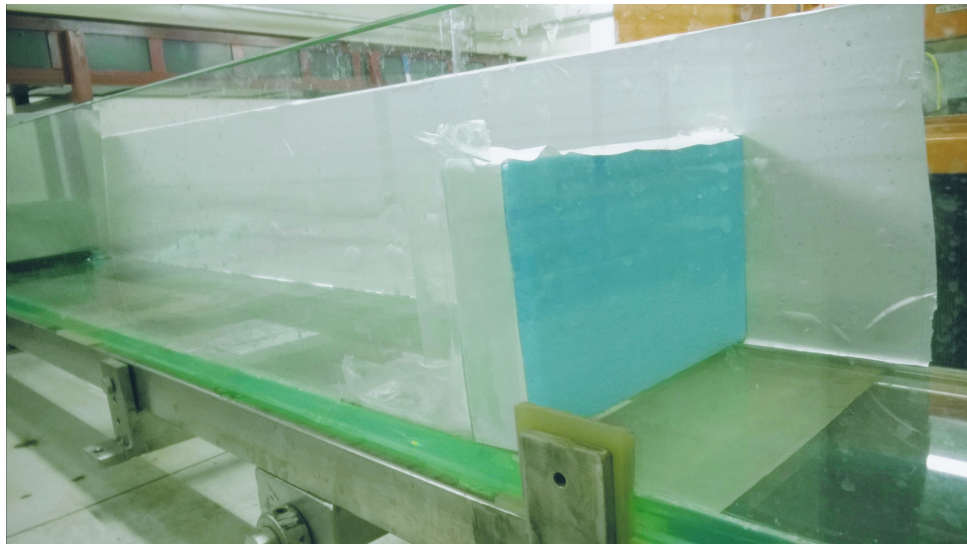


Figure 4.1: Empty wave tank, blocked off at 1.5 m.

The coastal defences were manufactured using the same modelling foam used to seal the tank. The benefit once again was that the structure could be made slightly larger, wedged in and taped to prevent movement and leakage. The five structures produced for the tank were the vertical wall, a 1:2 slope, a 1:3 slope, a 1:3 stepped slope and a re-curve. A schematic of the defences used is shown in figure 4.2. Images of each coastal defence with dimensions is shown in Appendix A. The coastal defences and their sizes were decided upon as a result of preliminary tests with the tank and with previous knowledge of sea defence design, as detailed in section 1.4.

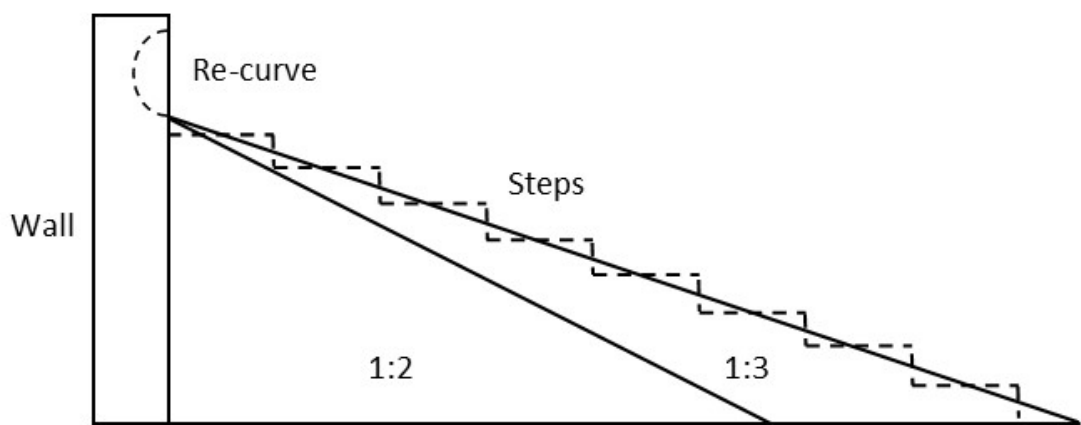


Figure 4.2: Schematic of coastal defences.

4.2 Wave Maker

4.2.1 Mechanical Design

A number of design iterations for the wave maker were realised with the aim of determining the most appropriate for the application. A review of waves and their production was provided in section 1.2. The first wave maker produced was a simple hand-operated wooden paddle hinged onto a base plate as shown in Appendix B. This allowed simple waves to be produced in the tank to get a feel for the magnitude while a more sophisticated wave maker was built.

It was shown in section 1.2 that a wave paddle hinged at the bottom of the tank would be advantageous in producing deep water waves where particle motion is generally circular in nature, however it would be unsuitable for producing shallow water waves. Regardless, due to its simplicity a prototype hinged wavemaker was produced and connected to a motor which would provide a constant angular velocity, as shown in figure in Appendix C. The drive mechanism was such that the amplitude could be changed by modifying the position of the connecting rod on the motor cam. It was found that the drive mechanism was inadequate for producing large amplitude rotations, mainly due to limitations on the length of the motor cam and connecting rod. Furthermore, even if the paddle was driven by hand it was difficult to produce waves of the required amplitude for overtopping, reinforcing the idea that this type of paddle would be better suited to producing deep water waves.

It was known that a piston-type wave maker would be more advantageous in shallower water where the aim was to model translational waves which would interact with structures. A design was conceived in which a flat paddle was connected to a set of rollers mounted horizontally. The paddle would then be connected to a motor with a similar drive mechanism to that used for the hinged paddle wave maker. However manufacturing and time constraints meant that this design would have been difficult to realise. Furthermore the nature of the design meant that amplitude modifications would involve altering the drive mechanism. A design with more control was desired for testing the wave tank under many different conditions so a third option was investigated.

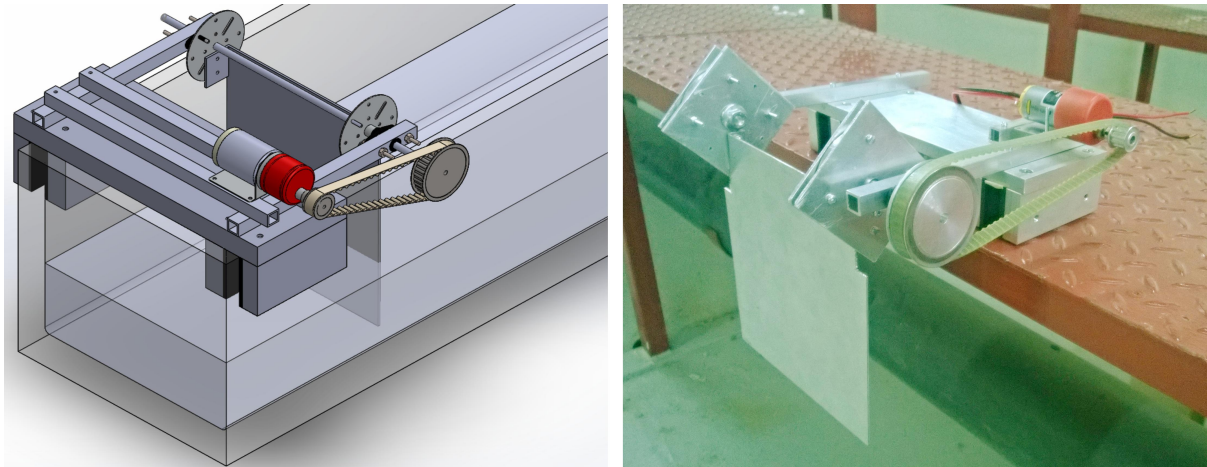


Figure 4.3: 3D CAD model and manufactured hinged wavemaker.

A paddle hinged above the free surface would allow direct rotational actuation from the motor, as opposed to a conversion of rotational into linear motion seen in the previous two designs. This would then allow the amplitude and frequency of the wave maker to be set via a control system, as described in Section 4.2.2. The initial design for a hinged wave maker involved connecting the motor to a pulley system, allowing an increased torque and reduced speed to be transferred to the wave paddle. The extra torque would be necessary in order to overcome the inherent inertia in the system. The 3D CAD model of this design and the manufactured model are shown in Figure 4.3. It was known that such a wave maker would not optimally simulate particle motion as it would attempt to increase orbits with depth. However upon testing it was found that amplitudes required for overtopping were easily achieved and the waves were ideal as a visual tool.

A control system was developed and this design was used during initial tests and in designing coastal defences. Excess movement was observed in the pulley system due to a slack belt and unsatisfactory connection between gears and shafts. These sources of inefficiency, along with the large size of the paddle resulted in undesirable movements when impacted by reflected waves. Therefore a final design iteration saw an improvement in mechanical efficiency by removing the pulley system and using a motor with a higher gear ratio fixed directly onto the paddle shaft. This design is shown in Appendix D and was used to obtain experimental data due to its robust and highly repeatable motion.

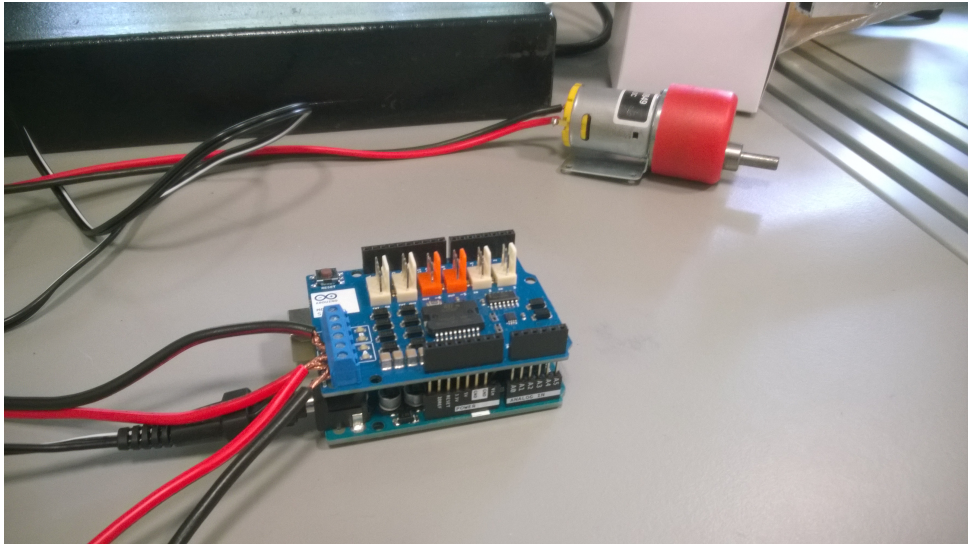


Figure 4.4: Arduino Uno with motor shield, connected to power supply and motor.

4.2.2 Control System

A control system for the wave maker was created using an open source microprocessor called an Arduino. The Arduino software uses a set of C/C++ functions which can be called from the code to run a motor, or receive data from a sensor for instance (Arduino, 2015a). An Arduino Uno was used as the main board to which the program would be uploaded. An Arduino motor shield was then used to interface the board to a motor. This was necessary as the outputs of the Uno board provided logic voltage and amperage of +/- 5V and 40 mA, whereas the shield allowed the motor to be driven using an external power supply providing the required 12 V / 2 A. The Arduino motor shield was mounted directly on top of the Uno board and was connected to the motor and power supply as shown in Figure 4.4. It must be noted that the V_{out} pin on the motor shield was removed and not connected to that of the Uno as it received power only from the power supply.

The Arduino featured 14 digital I/O pins, 6 of which provided Pulse Width Modulation (PWM) output. PWM is a technique for modulating the voltage between 0 V (off) and 5 V (on) by changing the length of time a digital pulse is sent, on a scale of 0 - 255 (Arduino, 2015b). As DC motor speed varies linearly with voltage after completing an acceleration period (Toliyat and Kliman, 2004), PWM allowed accurate control of the motor using the Arduino software. The motor was initially programmed to rotate in one direction for half the defined period, before breaking and returning to its original

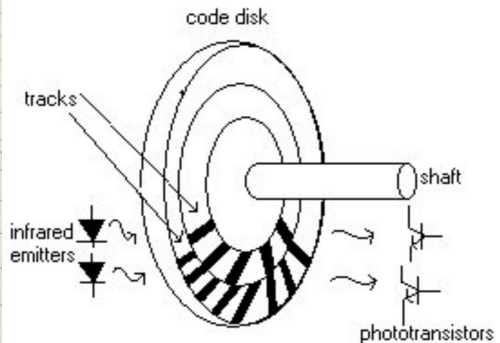
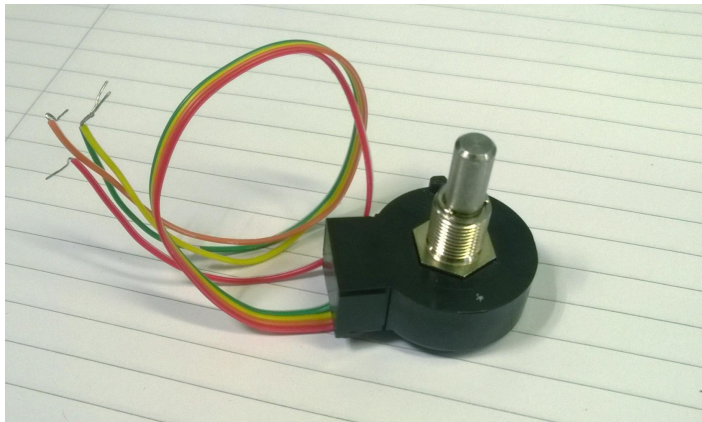


Fig 1. A rotary optical encoder

Figure 4.5: Optical encoder with schematic diagram

position. This was repeated for the desired number of periods. The code for this simple program is included in Appendix E. This program was found to be ideal for producing different waves as the period was defined within the program and desired amplitude was achieved by modifying either the PWM or the output voltage of the power supply.

The magnitude of the wave maker rotation was required when performing experiments as this would allow the same amplitude to be programmed into the SPH wave maker. Therefore the program was modified to take readings from an incremental optical encoder. Such an encoder consists of a clear disc marked with two sets of linearly spaced tracks. As the radial lines interrupt a beam between a photoemitter-detector pair, digital pulses are produced (Alciatore and Histand, 2011). The encoder used is shown in Figure 4.5 along with a schematic diagram.

Four wires were connected between the encoder and the Arduino, two of which were V_{in} and ground. The remaining wires connected the two phototransistors to I/O ports on the arduino, say channels ‘A’ and ‘B’ for namesake. A program was written to monitor encoder channels and increment or decrement a number whenever a pulse was received from channel ‘A’. Direction was determined by recording and looking at the previous state (HIGH/LOW) of channel ‘B’, in which pulses were slightly offset from those in channel ‘A’. A more detailed description of this method was provided by Alciatore and Histand (2011). This method of computing the data from an encoder had ‘1X’ resolution, meaning a single increment was recorded whenever channel ‘A’ became HIGH. The number

of pulses per revolution with this encoder was 128, therefore each pulse represented an angle of 2.813° . Twice the resolution, ‘X2’ could be achieved by taking readings whenever a channel switched both on and off, and four times the resolution by monitoring both channels. However ‘1X’ was considered a reasonable resolution since there would be other inaccuracies due mechanical movement, and it was difficult to keep the encoder in place while taking readings. Furthermore it was a cheap and fast algorithm so would interfere minimally with the program timing. The program used for encoder readings is shown in Appendix F.

The changes made to the program to incorporate an optical encoder also allowed more complex, time-dependent motions to be obtained with the motor, for instance a sinusoidal velocity signal, $V = \sin(\omega t)$. This was tested in the tank and little benefit was found in terms of waves and overtopping produced. In fact the waves were lower in amplitude due to the ramp-up and ramp-down of velocity. Therefore a simple on/off signal for the voltage and thus velocity was used. Figure 4.6 shows position of the encoder over time recorded after 5 periods during the experiment for a wave period of 1.25 s. The position after 5 periods was of particular interest as the effect of waves reflected off the coastal defence could be observed. As the paddle was moving forwards (sloping up), there was

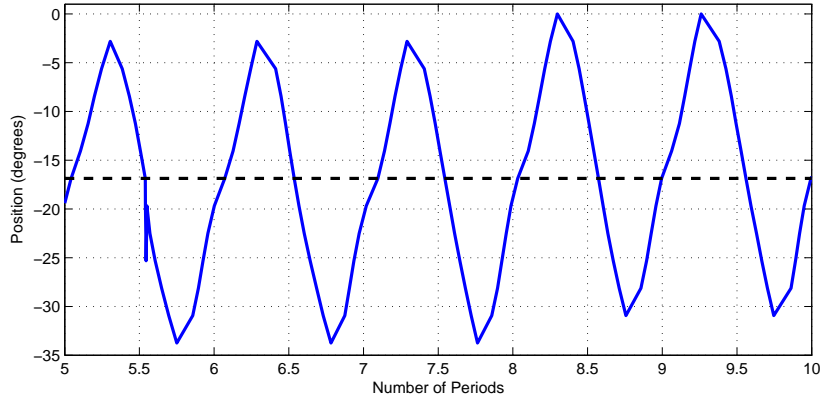


Figure 4.6: Encoder position against time as tested in the wave tank with period 1.25s.

a reduced velocity mid-way through the rotation. This was due to the reflected wave and meant that after a number of concurrent tests the wavemaker position had to be corrected. However it did not appear to have a significant effect on the waves produced and the paddle was re-aligned after each run.

Slight drifts in the oscillation were observed as in Figure 4.6. This was likely because the encoder was held in place largely by hand and any movement would effect the readings. This, along with the low resolution meant that encoder measurements were taken over 9 different experiments and averaged to obtain the amplitude. The mean amplitude was then determined to be 31° with a maximum error of 2.18° , or 1 increment.

4.3 Image processing

Videos of the experiments were analysed using image processing to extract the free-surface profile. During the experiments the back wall of the tank was covered in white plastic and the water was dyed black to produce a contrast. Frames of video were isolated, converted into greyscale and individual pixels were assigned either a 1 or 0 depending on whether they were light or dark. A script written in Matlab then extracted the location of the interface between 1s and 0s, i.e. the free surface. This was then compared to the free-surface profile obtained using SPH.

4.4 Experimental Design

Experiments were performed for each of the coastal defences shown in appendix A under continuous wave conditions with wavelength of 1m and period of 1.25 s. This wave period was chosen using a non-integer value of m in calculations of wavenumber, $\kappa = m\pi/L$ for $L = 1.3$ (working length), to avoid resonance. In this case a value of $m = 1.5$ resulted in $T = 1.29$ s, however tests showed that $T = 1.25$ s produced better visual results of discharge. Overtopping and free surface were recorded for 15 periods and experiments were repeated three times. Each coastal defence was also tested with a single wave to obtain images of the overtopping.

A standing wave was produced by choosing an integer value of m . In this case $m = 4$ resulted in two standing wave peaks and a period of 0.845 s. Therefore this period was programmed into the wave maker with a low amplitude such that the resonance could grow. The free surface was monitored but no overtopping was recorded.

Chapter 5

Results and Discussion

The overtopping was recorded for each coastal defence over 15 wave periods to determine the effect of each. This data is presented in table 5.1 along with the overtopping data obtained from SPH simulations.

Table 5.1: Overtopping of Experiment and SPH simulations.

Defence	Mean Overtopping (ml)	
	Experiment	SPH
Vertical Wall	502	26.5
Recurve	48	24.8
1:2 Slope	415	0
1:3 Slope	431	0
Steps	48	0

The SPH simulations were found to produce significantly less overtopping than the experiments, with zero overtopping predicted for the slopes and steps. This may have been due to the inherent damping in the system or as speculated by Van Alwon (2015) due to the particle spacing and artificial viscosity values used. Regardless, the experiments showed that coastal defences worked as expected. The most overtopping was observed with the vertical wall at 502 ml, while both the recurve and steps reduced this to 48 ml. Both slopes produced less overtopping than the vertical wall and the 1:3 slope showed slightly more overtopping than the 1:2 slope, as predicted in section 2.2. Figure 5.1 shows the overtopping pattern for each structure.

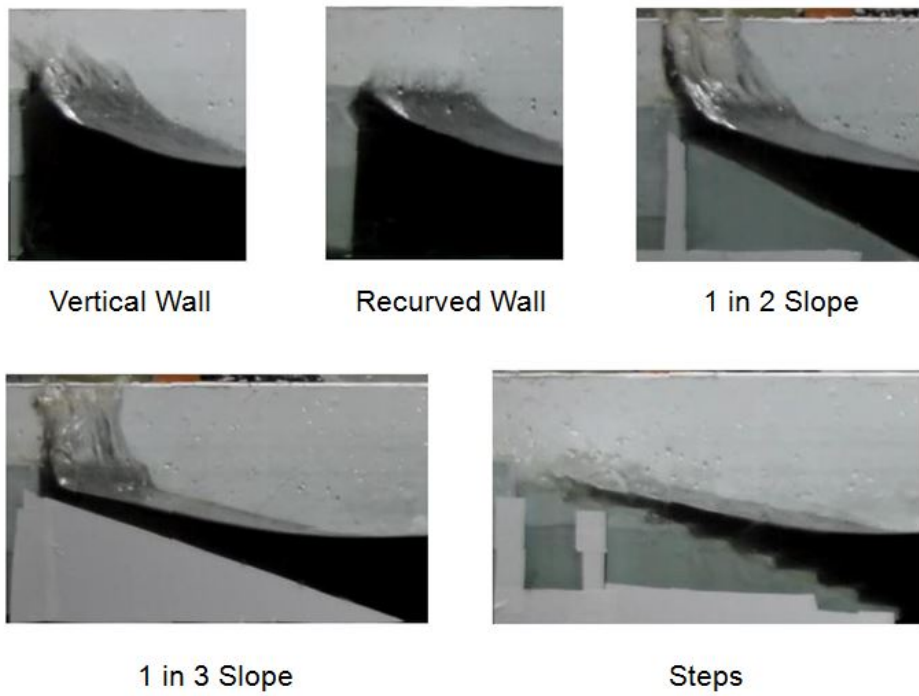


Figure 5.1: Images of Overtopping for Each Coastal Defence

The vertical wall exhibited both splashing and green-water overtopping indicating the wave energy impacting the wall was high and had not been dissipated beforehand. The recurve was seen to deflect the majority of the water seaward as expected, with a little overtopping due to splash. With no other defence present the recurve performed exceptionally well, suggesting it would be a good addition to any coastal defence. The slopes acted as ramps, producing more ‘green water’ overtopping with very little splash. This would be undesirable for use as a defence on its own, however when tested with the recurred wall (no measurements taken) the overtopping was reduced to zero. This was as expected because the slope directed the run-up efficiently into the curve, while also dissipating some of the energy, reducing splash. The steps also performed well on their own, effectively dissipating energy through turbulence. Although no green-water overtopping was observed the turbulence resulted in a lot of splashing, so it was not as efficient as the slope when tested with the recurve.

The repeatability of experiments was evaluated using free-surface profiles. Figure 5.2 shows the free-surface profile at a time of 17.8 s (16 wave periods) for three experiments.

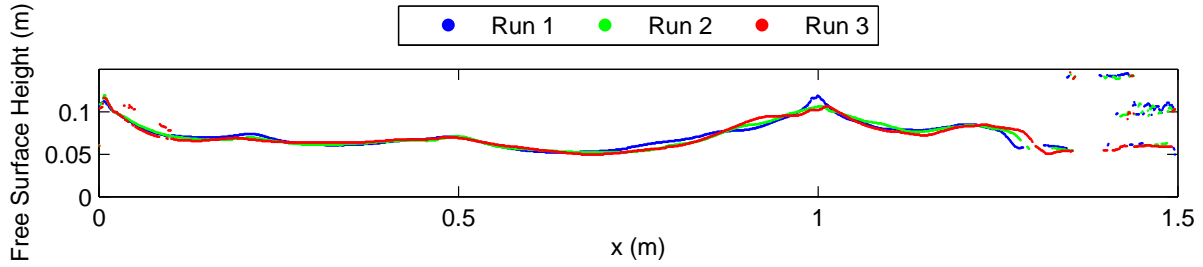


Figure 5.2: Free surface of waves impacting vertical wall at 17.8 s for three experimental runs.

It was seen that after 16 wave periods the free surface was approximated well, with a wave breaking at 1 m due to reflected waves and overtopping at the structure. This was evaluated at different times and found to be the same. The anomalous data behind the wave maker was due to shadows picked up during image processing. This suggested that the wave generator worked reliably and consistently.

Figure 5.3 shows an image of a standing wave after 13.8 seconds (16 periods). The free surface of this image was extracted using image processing and compared against the corresponding SPH data as shown in Figure 5.4. The comparison showed that the peaks closer to the defence matched reasonably well, whereas the peaks leaving the wavemaker did not. This could have been due to the damping in the system - if the returning wave was lower in amplitude in the SPH case, the combined wave amplitude would also be lower. Furthermore significant ‘jetting’ was observed at the peaks of waves in the experiment. This was not present in the SPH simulations, again most likely because of damping in the system.

Figure 5.5 shows the amplitude of a single point in the middle of the tank over time for the standing wave. This showed that the damping present in SPH simulations resulted in a more gradual growth of oscillations than in the experiment, although the waves always remained in phase. Figure 5.6 shows a plot of potential energy in the SPH simulation, calculated using equation 3.1. Time constraints prevented obtaining full time-series data for the experimental free-surface, however it would be interesting to plot the energy during the experiment in future work.



Figure 5.3: Image of standing wave after 16 wave periods.

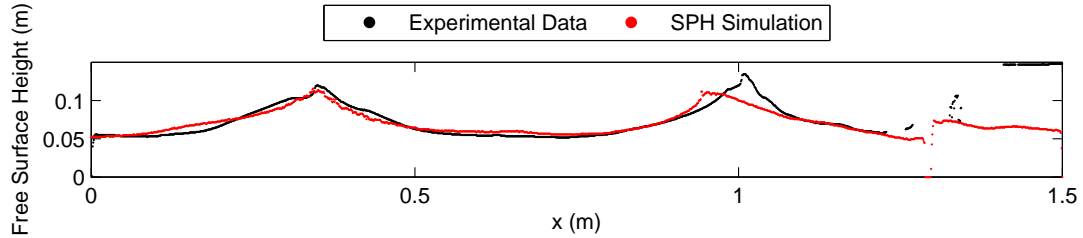


Figure 5.4: Comparison of experimental and SPH free-surface profiles for standing wave after 16 periods.

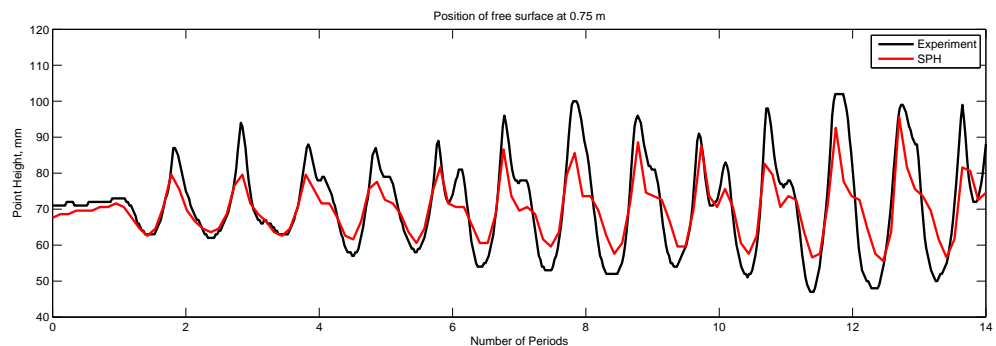


Figure 5.5: Comparison of height of a single point in the centre of the domain over time for SPH simulations and experiment.

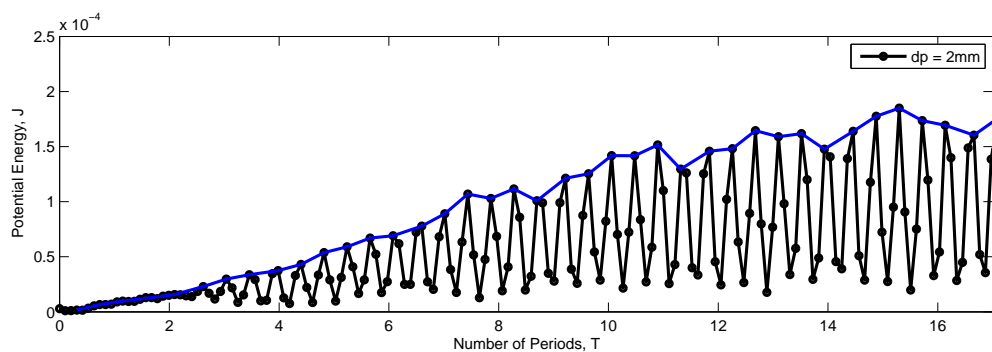


Figure 5.6: Energy growth in SPH simulation for a standing wave.

The energy was observed to gradually increase and level out at around 15 wave periods, fluctuating thereafter. The reason it stopped growing in SPH was likely because of damping as no overtopping was observed. In the experimental tank, energy loss due to jetting along with periodic overtopping removed energy from the system, stopping it from growing any further.

5.1 Conclusions

The wave maker was found to be highly reliable and produced consistent experimental results, though improvements could be made in reducing the effect of inertia on the forward stroke. This could be achieved by using a higher powered motor – though this would also require a higher powered Arduino. Comparison of SPH to linear theory revealed that potential energy in the solutions damped by half over two wave periods. The damping present in the SPH simulations may have resulted in lower amounts of overtopping recorded however this could also have been due to particle spacing or viscosity. Furthermore the damping prevented the energy in the system from growing when forced at standing wave frequency and also damped out any ‘jetting’ which was observed in experiments. Overall the free-surface profiles predicted by SPH were good approximations to those obtained in experiments.

Experiments informed the design of a final tank to be manufactured by HydroTec Consultants Ltd and delivered to JBA. The wavemaker will use the same motor, drive mechanism and control system as used in the experiments, as will the coastal defence profiles. However the practicalities of removing and changing defences will be designed by HydroTec, along with adjustable feet for levelling, an overhead hopper for replacing water and a tap for siphoning overtopped water for comparison, as shown in Appendix G. The design for JBA will also include buttons and switches connected to the Arduino to change wave conditions without accessing the program. This will require calibration but will improve the overall quality and usability of the wave tank.

Bibliography

- Alciatore, D. G. and Histand, M. B. (2011). *Introduction to Mechatronics and Measurement Systems, 4th Ed.* McGraw Hill, USA.
- Arduino (2015a). *Arduino FAQ*. <http://www.arduino.cc/en/Main/FAQ>.
- Arduino (2015b). *Arduino Learning: PWM*. <http://www.arduino.cc/en/Tutorial/PWM>.
- Biesel, F. (1948). Le filtre a houle systeme neyrcpic. *La Houille Blanche, No. 3*.
- Chappell, E. R. (1953). Theory and design of a wave generator for a short flume. *Masters Thesis, Department of Civil Engineering*.
- Crespo, A., M., G.-G., and Dalrymple, R. (2008). Modeling dam break behaviour over a wet bed by a sph technique. *Journal of Waterway, Port, Coastal, and Ocean Engineering, 134(6)*.
- Dalrymple, R. and Rogers, B. (2006). Numerical modeling of water waves with the sph method. *Coastal Engineering, 53*.
- Deltares (2015). *Overtopping Neural Network*. <https://www.deltares.nl/en/software/overtopping-neural-network/>.
- Edinburgh Designs (2015). *Wave Generators*. <http://www.edesign.co.uk/waves/some-wave-1/>.
- Goda, Y. (2010). *Random Seas and Design of Maritime Structures*. World Scientific Publishing Co. Pte. Ltd., Singapore.
- Gomez-Gesteira, M. and Dalrymple, R. (2004). Using a 3d sph method for wave impact on tall structure. *Journal of Waterway, Port, Coastal, and Ocean Engineering, 130(2)*.

- Gomez-Gesteira, M., Rogers, B., and Crespo, A. (2010). State-of-the-art of classical sph for free-surface flows. *Journal of Hydraulic Research*, 48 Extra Issue.
- Gomez-Gesteira, M., Rogers, B., Crespo, A., Dalrymple, R., Narayanaswamy, M., and Dominguez, J. (2012). Sphysics - development of a free-surface fluid solver - part 1: Theory and formulations. *Computers and Geosciences*.
- Hofmann, H. (2008). *Characteristics and Implications of Surface Gravity Waves in the Littoral Zone of a Large Lake*. Cuvillier Verlag Gottingen, Germany.
- HR Wallingford (2007). *EurOtop, Wave Overtopping of Sea Defenses and Related Structures: Assessment Manual*. Boyens Medien GmbH & Co., Holstein, Germany.
- Ippen, A. T. and Eagleson, P. S. (1966). *Estuary and Coastline Hydrodynamics*. Massachusetts Institute of Technology, Hydrodynamics Laboratory, USA.
- JBA (2015). *Homepage*. url: <http://www.jbatrust.org/> accessed: 2015-06-08.
- Keulegan, G. (1966). The approximate theories of pneumatic wave generators. *U.S. Army Engineer Waterways Experiment Station*.
- Lighthill, J. (1978). *Waves in Fluids*. Cambridge University Press, Cambridge, UK.
- Munk, W. H. (1950). Origin and generation of waves. In *Proceedings of First Conference on Coastal Engineering*, Long Beach, California.
- Owen, M. (1980). Design of seawalls allowing for wave overtopping. *HR Wallingford Report*.
- Straub, L. G. and Pilch, M. (1953). Laboratory wave-generating apparatus. *St Anthony Falls Hydraulic Laboratory, Report no. 39*.
- Thomas, R. and Hall, B. (1992). *Seawall Design*. Butterworth HeinemannLtd., Oxford, UK.
- Toliyat, H. A. and Kliman, G. B. (2004). *Handbook of Electric Motors*. Marcel Dekker, Inc., USA.
- Tsuruta, S. and Goda, Y. (1968). Expected discharge of irregular wave overtopping. In *Hydraulics Division, Port and Harbour Research Institute*, Tokyo, Japan.

Van Alwon, J. (2015). *MSc Thesis: Experimental and Numerical Modelling of Coastal Processes*. University of Leeds, United Kingdom.

Van der Meer, J., Bruce, T., Allsop, N., Franco, L., Kortenhaus, A., Pullen, T., and Schuttrumpf, H. (2013). Eurotop revisited. part 1: Sloping structures. In *Proc. ICE, Coasts, Marine Structures and Breakwaters*, Edinburgh, UK.

Appendix A

Coastal Defences

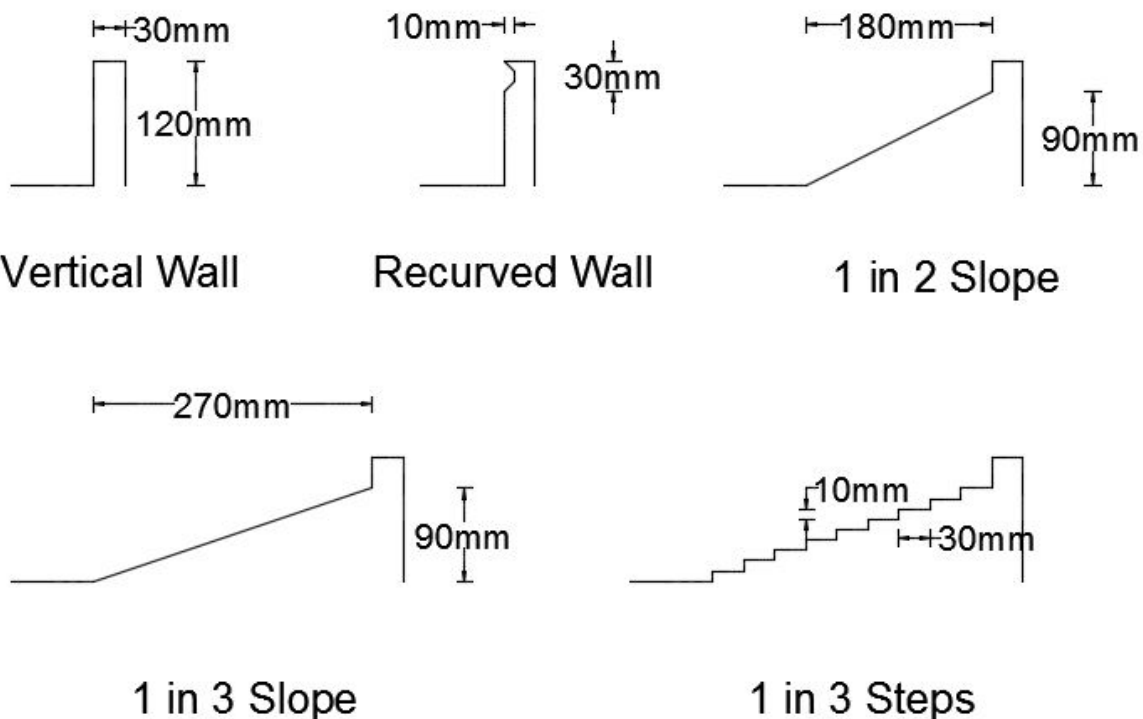


Figure A.1: Coastal defences used in experiments with dimensions.

Appendix B

Wood Paddle

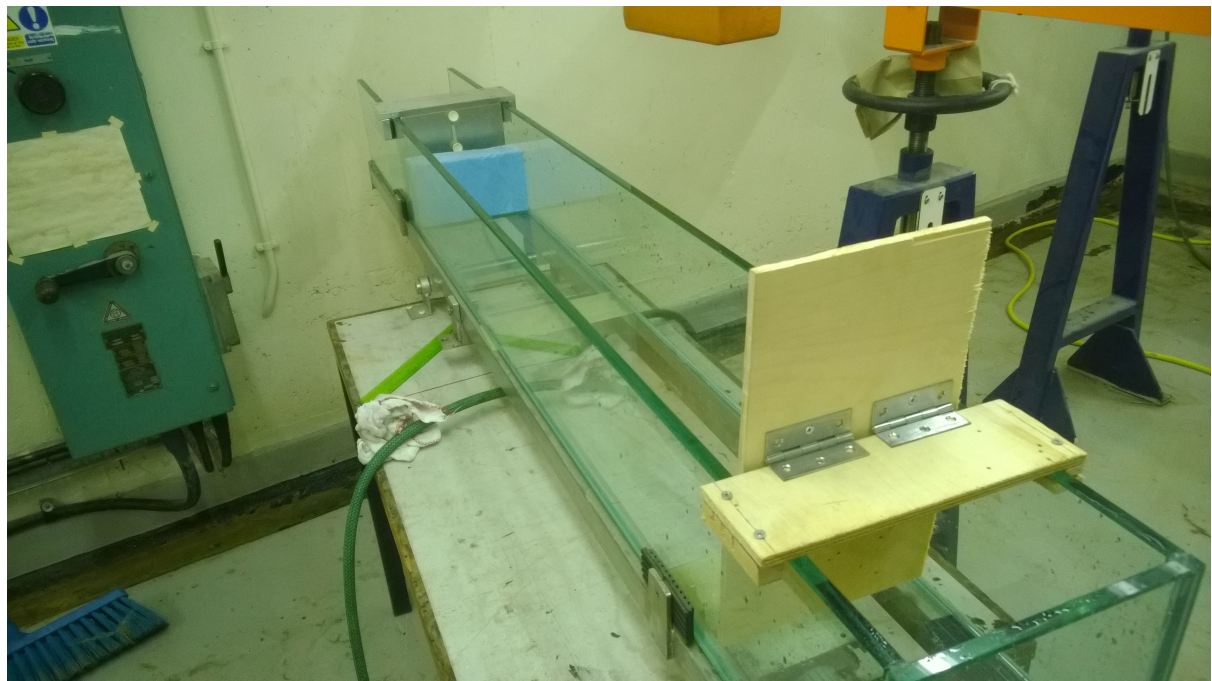


Figure B.1: Make-shift wood paddle hinged on a baseplate.

Appendix C

Paddle Hinged at Bottom



Figure C.1: Wave maker with paddle hinged on floor of tank.

Appendix D

Improved Wave Maker

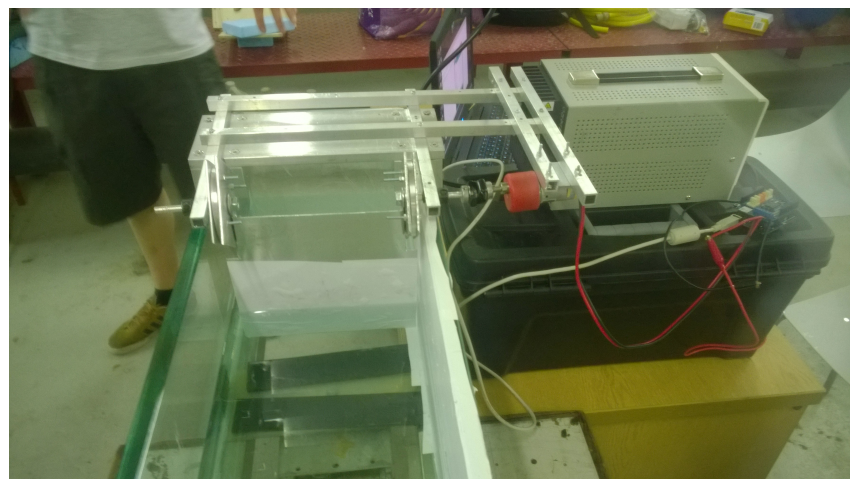


Figure D.1: Modified wave maker image 1.



Figure D.2: Modified wave maker image 2.

Appendix E

Simple Arduino Program

```
// Set constants
const int
PWM_A    = 3,
DIR_A    = 12,
BRAKE_A = 9,
SNS_A    = A0;
int counter = 0;
int counter_lim = 10;
int pwm = 255;
int period = 1600;

void setup() {
//MOTOR
// Configure the A output
pinMode(BRAKE_A, OUTPUT); // Brake pin on channel A
pinMode(DIR_A, OUTPUT);   // Direction pin on channel A

// Open Serial communication
Serial.begin(9600);
Serial.println("Motor shield DC motor Test:\n");
}

void loop() {

// Run half a loop forward
if(counter <1){
digitalWrite(BRAKE_A, LOW); // setting brake LOW disable
digitalWrite(DIR_A, HIGH); // setting direction to forward

analogWrite(PWM_A, pwm); // Set the speed of the motor,
delay(period/4); // hold the mototr full speed
digitalWrite(BRAKE_A, HIGH);
}

// Run back and forth until counter = counter lim (no. of periods).
```

```

if(counter<counter_lim){
    digitalWrite(BRAKE_A, LOW); //
    digitalWrite(DIR_A, LOW);   //
    analogWrite(PWM_A, pwm);    //
    delay(period/2);           // run for half period

    // Brake the motor
    // raising the brake pin the motor will stop faster
    digitalWrite(BRAKE_A, HIGH); // raise the brake

    // Set the outputs to run the motor backward
    digitalWrite(BRAKE_A, LOW); //
    digitalWrite(DIR_A, HIGH);
    analogWrite(PWM_A, pwm);    // Set the speed of the motor
    delay(period/2);           // run for half a period

    // Brake
    digitalWrite(BRAKE_A, HIGH); // raise the brake

    counter = counter + 1;    // increment counter (no. periods).
}

// Run half a loop backward when period limit reached
if(counter == counter_lim){
    digitalWrite(BRAKE_A, LOW); // setting brake
    digitalWrite(DIR_A, LOW); // setting direction

    analogWrite(PWM_A, pwm); //
    delay(period/4);
    digitalWrite(BRAKE_A, HIGH);
    counter = counter + 1;
}

}

```

Appendix F

Encoder Code

```
/* Read Quadrature Encoder
 * Connect Encoder to Pins encoderPinA, encoderPinB, and +5V.
 */
int val;
int encoderPinA = 2;
int encoderPinB = 4;
int encoderPos = 0;
int encoderPinALast = LOW;
int n = LOW;

void setup() {
    pinMode (encoderPinA,INPUT);
    pinMode (encoderPinB,INPUT);
    Serial.begin (9600);
}

void loop() {
    n = digitalRead(encoderPinA);
    if ((encoderPinALast == LOW) && (n == HIGH)) {
        if (digitalRead(encoderPinB) == LOW) {
            encoderPos--;
        } else {
            encoderPos++;
        }
        Serial.print (encoderPos);
        Serial.print ("\n");
    }
    encoderPinALast = n;
}
```

Appendix G

Final Design and Extra Defences

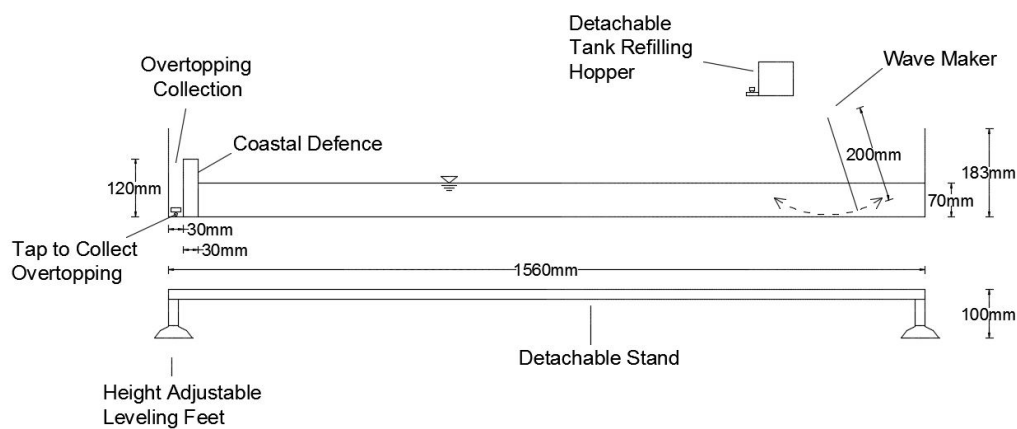


Figure G.1: Final tank design with extra functionality.

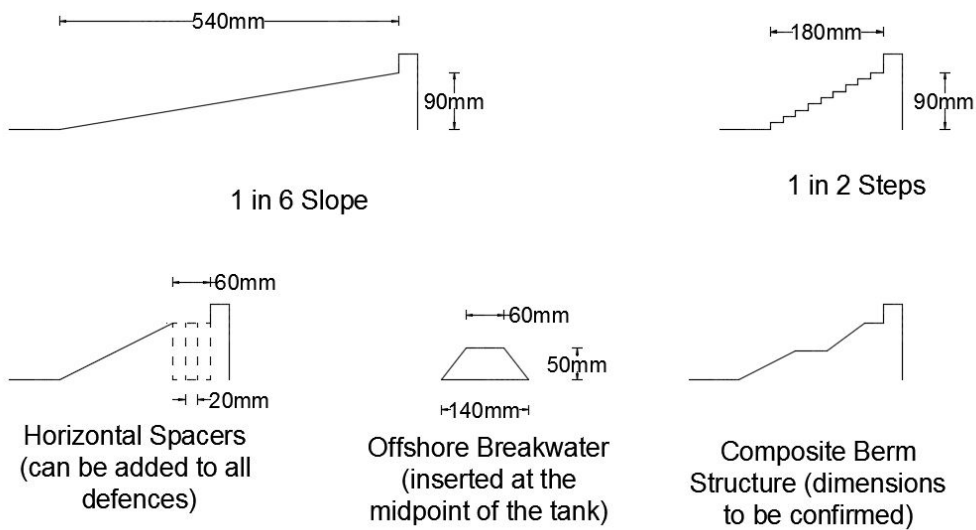


Figure G.2: Additional defences to be built for JBA.